IEEE Photonics Journal
An IEEE Photonics Society Publication

Open Access

Demonstration of 128-Channel Optical Phased Array With Large Scanning Range

Volume 13, Number 3, June 2021

Guangzhen Luo
Pengfei Wang
Jianbin Ma
Ruiting Wang
Zhengxia Yang
Yang Xu
Hongyan Yu
Xuliang Zhou
Yejin Zhang
Jiaoqing Pan

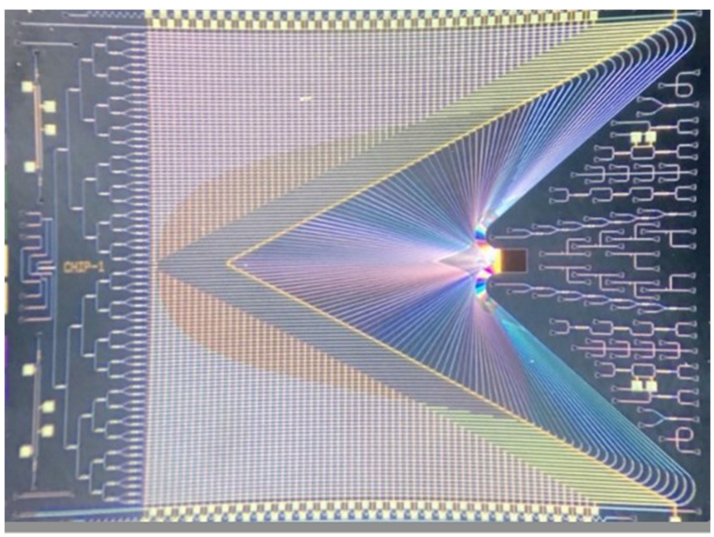

DOI: 10.1109/JPHOT.2021.3071185

IEEE photonics SOCIETY

IEEE

Demonstration of 128-Channel Optical Phased Array With Large Scanning Range

Guangzhen Luo,[1,2] **Pengfei Wang**,[1,2] **Jianbin Ma**,[1,2] **Ruiting Wang**,[1,2] **Zhengxia Yang**,[1,2] **Yang Xu**,[3] **Hongyan Yu**,[1,2] **Xuliang Zhou**,[1,2] **Yejin Zhang**,[1,2] **and Jiaoqing Pan**[1,2]

[1]Key Laboratory of Semiconductor Materials Science, Institute of Semiconductors, Chinese Academy of Sciences, Beijing 100083, China
[2]Center of Materials Science and Optoelectronics Engineering, University of Chinese Academy of Sciences, Beijing 100049, China
[3]Beijing R&D Institute, VanJee Technology, Beijing 100193, China

DOI:10.1109/JPHOT.2021.3071185

Manuscript received January 23, 2021; revised April 1, 2021; accepted April 1, 2021. Date of publication April 6, 2021; date of current version June 25, 2021. This work was supported in part by Natural Science Foundation of China under Grants 61934007 and 62090053, in part by Beijing Natural Science Foundation under Grant Z200006, in part by Beijing Municipal Science and Technology Project under Grant Z191100004819011, and in part by National Key R&D Program of China under Grant 2018YFE0203103. Corresponding author: Jiaoqing Pan (e-mail: jqpan@semi.ac.cn).

Abstract: We have proposed a 128-channel silicon-based optical phased array (OPA) chip with an overall antenna, and a large two-dimensional scanning range of 104.0° × 17.6° was achieved.

Index Terms: Optical beam-steering, OPA, Lidar.

1. Introduction

As an all-solid-state beam steering technology, optical phased array (OPA) is promising in light detection and ranging (LiDAR) fields, such as autonomous driving, three-dimensional imaging, and mapping. Many researches related to OPA have been reported [1]–[20], and it is widely considered to be a key sensing modality for reliable autonomous systems, most notably for self-driving cars [21]. OPA is also promising in the field of free space optical communications, and there have been some related reports in recent years [22]–[27]. Among various forms of OPA, silicon-based OPA is compatible with CMOS processes, and has the advantages of low cost and easy to hybrid integration of optical and electronic components.

For OPA-based sensing systems, in order to meet practical needs, a large scanning range is very important. In recent years, silicon-based OPA has achieved larger and larger steering angles [20], [24], [28]. Among them, Columbia University has achieved the largest steering angle (180°) by adopting an end-fire optical phased array with half-wavelength pitch [24]. However, it can only realize one-dimensional beam scanning, and will be limited in many applications.

In this paper, we have proposed a 128-channel OPA chip. A two-dimensional scanning is realized by a combination of phase modulation (in the lateral direction) and wavelength tuning (in the longitudinal direction). We have achieved a large scanning range of 104.0° in the lateral direction and 17.6° in the longitudinal direction, which can meet some two-dimensional scanning applications.

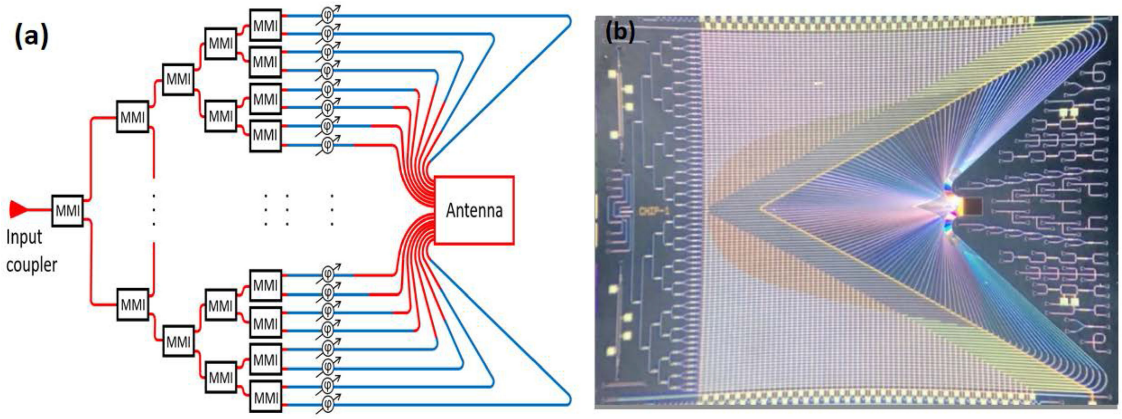

Fig. 1. (a) Diagram of the proposed OPA chip. (b) Photo of the proposed 128-channel OPA chip.

2. Structure and Characteristics

The schematic diagram and photo of the OPA chip are shown in Fig. 1(a) and Fig. 1(b), respectively. It consists of four parts: input coupler, optical beam splitters, phase shifters, and optical antenna. The input coupler is used to couple the laser beam to the chip. The optical beam splitters are used to divide the input beam into 128 channels. In this paper, we adopted the 1 $\times$ 2 multi-mode interference (MMI) tree as the optical beam splitters. The phase shifters are used to modulate the phase of beam in each optical waveguide. We adopted thermo-optic phase shifters to achieve phase adjustment. The optical antenna is used to emit beam into free space. We adopted the overall grating as the optical antenna for large scanning range, which is proposed in our previous work [11], [28]. When the OPA chip works, in the lateral direction, the light in each adjacent waveguide will have a same phase difference φ after being modulated by each phase shifter, and the beam will steer to a specific angle (Φ). Changing the value of φ, the steering angle of the beam will also change. In the longitudinal direction, the steering angle (Θ) of the beam will vary by tuning the wavelength. In this way, OPA realizes two-dimensional scanning.

We designed two type of 128-channel OPA chips with different input waveguide spacing (2 μm and 1 μm) at the antenna for comparison, named Chip1 and Chip2, respectively. They have the same structure except for the input waveguide spacing.

Due to the limitation of the MPW block size (6 mm $\times$ 8 mm), we designed the outer waveguide to be folded back. Since the outer waveguides are longer than the middle ones, the beams in these waveguides have different losses before the antenna, which is very detrimental to the scanning characteristics of the far-field spot. To solve this problem, we innovatively proposed a solution to adjust the optical loss of each waveguide by adopting a combination of ridge waveguide and strip waveguide. The loss of ridge waveguide is 1 dB/cm and the loss of strip waveguide is 1.5 dB/cm. As shown in Fig. 1(a), the blue waveguide represents the ridge waveguide and the red waveguide represents the strip waveguide. In order to demonstrate the effectiveness of this solution, we carried out a simulation of 16-channel OPA, which is the same type as the 128-channel OPA proposed by us. When the phase difference φ between the waveguides is 0°, the far-field spots before and after adopting this solution are shown in Fig. 2(a) and Fig. 2(b), respectively. When φ is 180°, the far-field spots before and after adopting this solution are shown in Fig. 2(c) and Fig. 2(d), respectively. Obviously, by adopting this solution, the divergence angle of the light spot in the lateral direction is smaller. Moreover, the light intensity has increased by an order of magnitude.

We adopted thermo-optic phase shifters to achieve phase adjustment, as shown in Fig. 3(a). A high-resistivity TiN material with a length of 800um is placed above the silicon waveguide with 2 μm SiO_2 spacing. In order to characterize the performance of the phase shifters, we fabricated a Mach-Zehnder (MZ) modulator on the chip, as shown in Fig. 3(b).

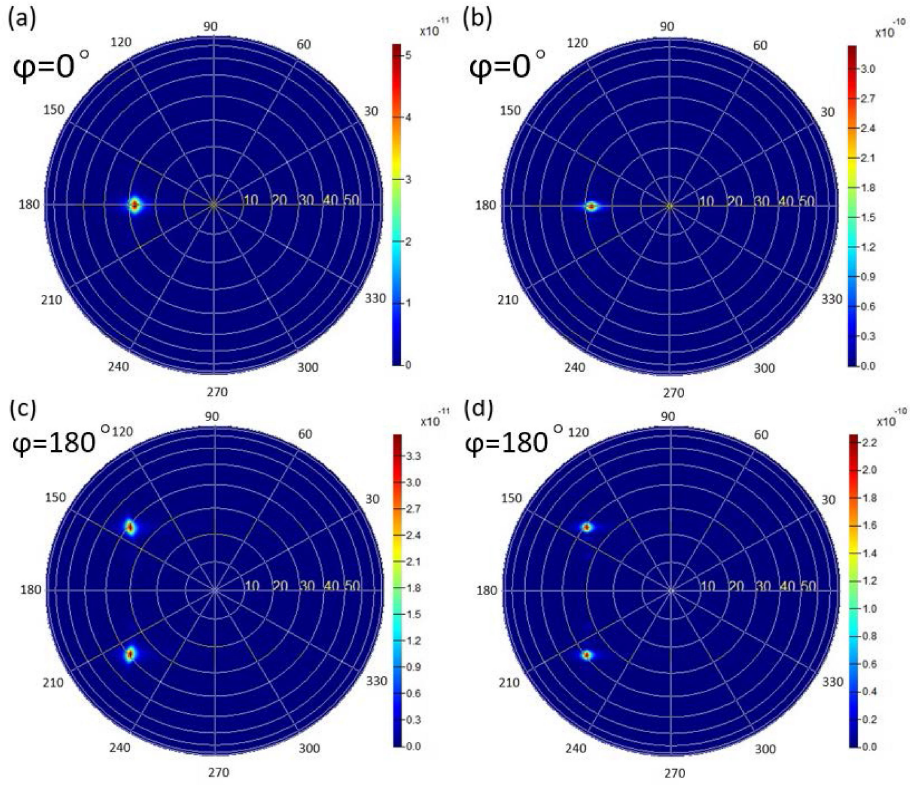

Fig. 2. Far-field radiation simulation results. (a) Only one type of waveguides and φ is 0°. (b) Combining ridge waveguides and strip waveguides, and φ is 0°. (c) Only one type of waveguides and φ is 180°. (d) Combining ridge waveguides and strip waveguides, and φ is 180°.

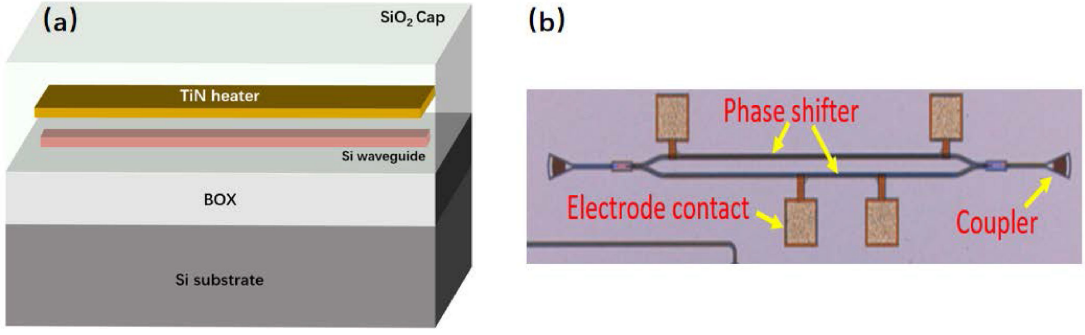

Fig. 3. (a) Schematic of the thermo-optic phase shifter. (b) Photo of the MZ modulator.

For our optical antennas, all waveguides share one antenna, and the input light interferes in the grating area and then emits outward. So there is no need to consider the problem of crosstalk. The schematic and the photo of the optical antenna are shown in Fig. 4(a) and Fig.4(b). The grating is fabricated on a wide Si slab, the grating period is 470 nm, the duty cycle is 50%, and the etching depth is 70 nm. The simulation performance of the antenna can be found in our previous papers [28], and this paper will not repeat it.

Before being fabricated, we simulated the two-dimensional scanning range of Chip1 and Chip2 in the wavelength range of 1480–1580 nm. Since the grating period and duty ratio of these two

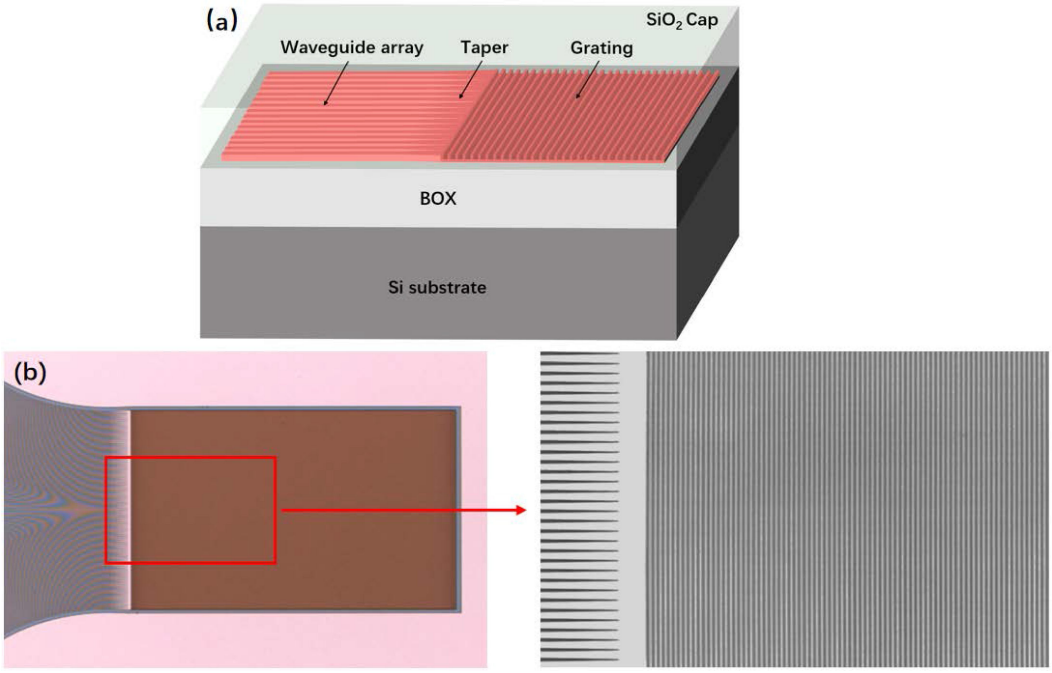

Fig. 4. (a) Schematic of the optical antenna. (b) Photo of the optical antenna.

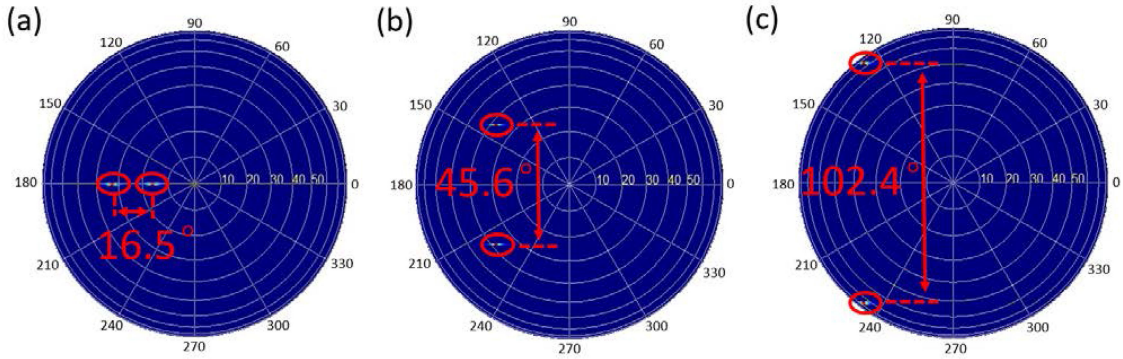

Fig. 5. (a) Scanning range of Chip1 and Chip2 in the longitudinal direction. (b) Scanning range of Chip1 in the lateral direction. (c) Scanning range of Chip2 in the lateral direction.

antennas are the same, their scanning ranges in the longitudinal direction (the wavelength tuning direction) are also the same, both of which are 16.5°, as shown in Fig. 5(a). In the lateral direction (the phase modulation direction), since the input waveguide spacing of Chip2 is smaller than that of Chip1, the scanning range of Chip2 is relatively large. As shown in Fig. 5(b) and Fig. 5(c), the scanning ranges of Chip1 and Chip2 in the lateral direction are 45.6° and 102.4°, respectively.

3. The Development of OPA Demo

When the OPA chip works, a drive circuit is required to provide a precise driving voltage for each thermo-optical phase shifter. In order to obtain the optimal emitted spot and achieve good scanning characteristics, the drive circuit is required to have high voltage accuracy, fast response and good

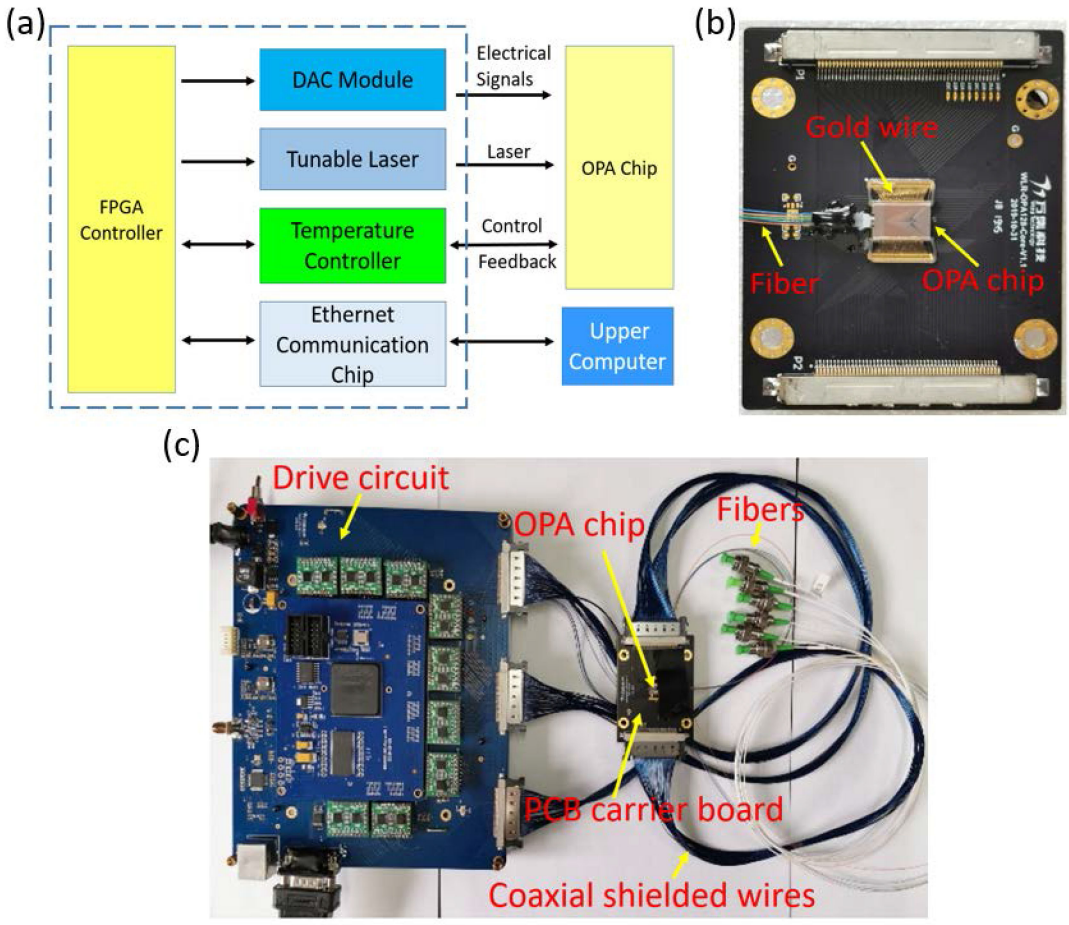

Fig. 6. (a) Schematic diagram of the OPA system. (b) Photo of packaged chip. (c) OPA demo.

synchronization between channels. We have developed a 128-channel drive circuit based on an FPGA chip. It provides voltage signals to each phase shifter of the OPA chip through digital-to-analog conversion (DAC), and has the advantages of high voltage accuracy, fast response and good synchronization. The schematic diagram of the entire OPA system is shown in Fig. 6(a).

Before testing, we packaged these two OPA chips. We bonded the chip to the PCB carrier board, and packaged the single-mode fiber to the input coupler of the chip, as shown in Fig. 6(b). When testing the OPA chip, the packaged chip will be connected to the drive circuit through coaxial shielded wires, and the drive circuit will provide voltage to each phase shifter.

The demo of the proposed OPA system is shown in Fig. 6(c). When it works, under the control of the upper computer, the drive circuit provides the voltage signals to modulate the phase of each channel. At the same time, the drive circuit also provides a synchronous trigger signal to the laser. In order to keep the chip working in a stable environment, the temperature controller works in real time.

4. Test Results and Analysis

We have built a scanning test system to test the scanning range of the main lobe. This system can be found in our previous paper [28]. We tested the phase optimization capability of the OPA demo. Through the stochastic gradient descent algorithm, the emitted beam can be optimized from the

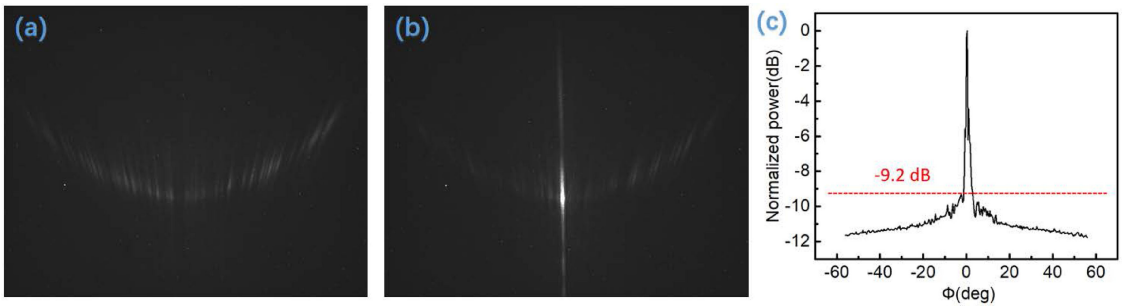

Fig. 7. (a) The emitted beam before optimization. (b) The emitted beam after optimization. (c) Far field intensity distribution.

scattered state to the converged state, as shown in Figs 7(a) and 7(b). After optimization, the side mode suppression ratio of the spot is more than 9.2 dB, as shown in Fig. 7(c).

According to the multi-slit diffraction model provided by Fourier Optics, for the diffraction peaks of each order (including zero-order and first-order) of the one-dimensional uniform grating, their light intensity, and the angular distance from the center of the screen will vary with the aforementioned phase difference φ between adjacent antenna elements. Here, we only discuss the peaks of zero- and first-orders, which are closely related to the OPA scanning range. When the absolute value of the phase difference $|\varphi|$ is less than π, the intensity of the zero-order peak will be stronger than that of the first-order peak. In this case, the zero-order peak and the first-order peak are the main lobe and grating lobe, respectively. In particular, when $\varphi = 0$, the zero-order peak will be located in the center of the screen, and its light intensity will be the strongest. In this case, the grating lobes will be completely suppressed. When $|\varphi|$ is greater than π, the zero-order peak will be farther from the center of the screen, and its light intensity will be weaker than that of the first-order peak. In this case, the first-order peak will replace the zero-order peak as the main lobe. When $|\varphi|$ is equal to π, the intensity of the zero-order peak and the first-order peak will be equal (that is, the intensity of the main lobe and the grating lobe will be equal), and their positions will be symmetrical about the center of the screen.

We tested the Chip1 first. Its input waveguide spacing of the antenna is 2 μm. Under the control of stochastic gradient descent algorithm, we used the scanning test system to optimize the light spots corresponding to each pixel in the wavelength range of 1480–1580 nm. We obtained clear and detailed light spots of diffraction peaks. And the light intensity and steering angle of each zero-order peak and first-order peak were consistent with the theory. Among them, at a wavelength of 1550 nm, several representative optimization results are shown in Fig. 8. In the figure, the light spots of the zero-order peak and the first-order peak are marked with a red dashed rectangle and a yellow dashed rectangle, respectively. On the whole, the light spots are distributed in an arc shape, which is consistent with the simulation results [28].

As shown in Fig. 8, when $|\varphi|$ decreases first (from Fig. 8(a) to Fig. 8(e)) and then increases (from Fig. 8(e) to Fig. 8(i)), the intensity and the angular distance from the center of the screen of the zero- and first-order peaks will change regularly. The zero-order peak will move from the left side of the screen (as shown in Fig. 8(a)) to the right side (as shown in Fig. 8(i)), and its light intensity first increases and then decreases. At the center of the screen, the zero-order peak has the strongest intensity (as shown in Fig. 8(e)). During the whole process, the first-order peak disappears first and then appears. We will describe in detail below.

When $|\varphi|$ is less than π, the intensity of the zero-order peak is stronger than that of the first-order peak. In this case, the zero-order peak is the main lobe, and the first-order peak is the grating lobe. In particular, when the value of $|\varphi|$ is within a specific numerical range, the grating lobes are completely suppressed, and there is only the main lobe (zero-order peak) on the screen, as shown in Fig. 8(d), (e), and (f). When $\varphi = 0$, the zero-order peak is located in the center of the screen.

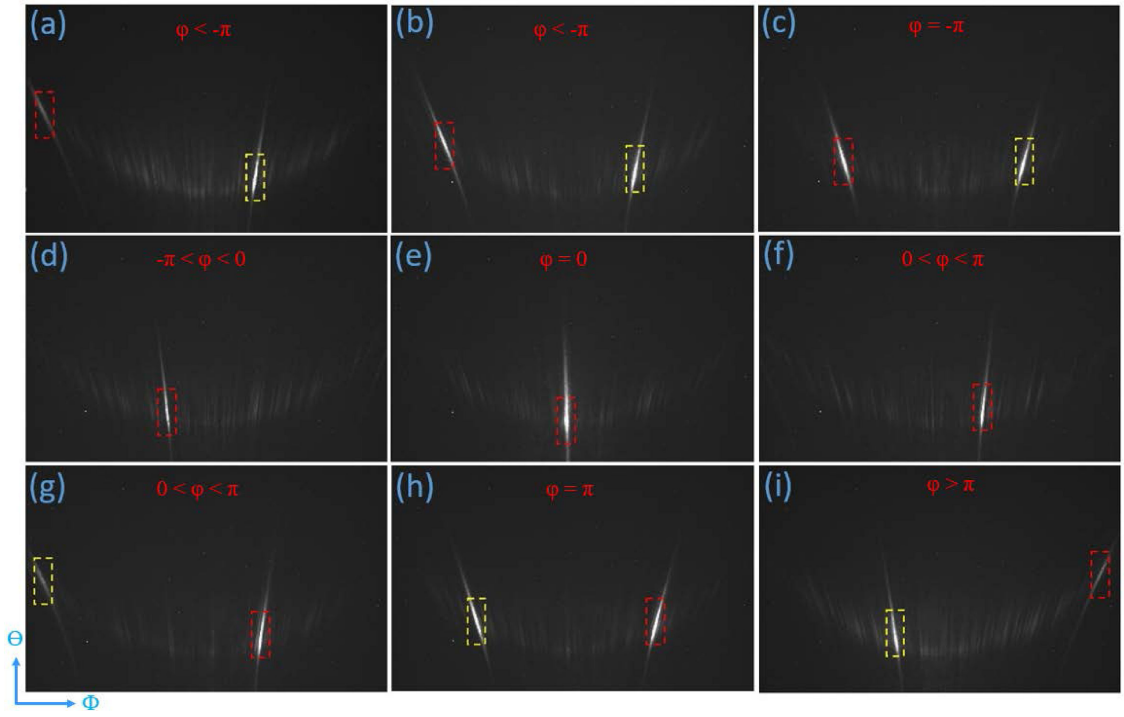

Fig. 8. Dynamic changes of zero-order and first-order diffraction peaks with different phase differences φ. The red dashed rectangle and yellow dashed rectangle correspond to the zero-order peak and the first-order peak, respectively.

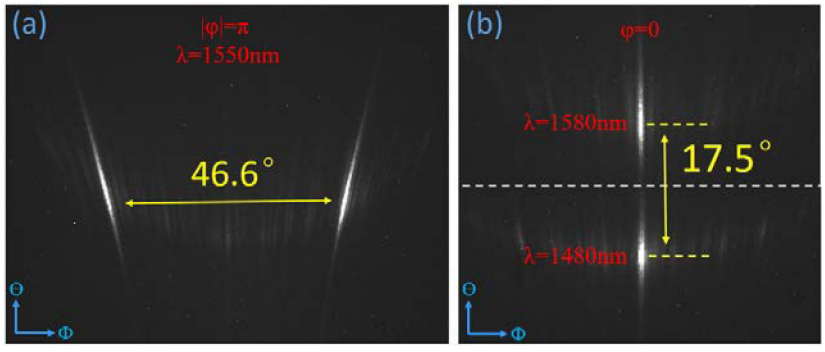

Fig. 9. (a) Lateral scanning range of Chip1. (b) Longitudinal scanning range of Chip1.

When $|\varphi|$ is greater than π, the zero-order peak is farther from the center of the screen, and its intensity is weaker than that of the first-order peak, as shown in Fig. 8(a), (b), and (i). In this case, the first-order peak will replace the zero-order peak as the main lobe. When $|\varphi| = \pi$, the positions of the zero-order peak and the first-order peak are symmetrical about the center of the screen, and their intensities are equal, as shown in Fig. 8(c)(φ = -π) and Fig. 8(h) ($\varphi = \pi$). In this case, the intensity of the main lobe and the grating lobe are equal, and the angular distance between them is the effective scanning range of OPA in the lateral direction.

Dynamically, when the value of φ is negative and $|\varphi|$ gradually decreases from a value greater than π to 0 (from Fig. 8(a) to (e)), the zero-order peak moves from the left side of the screen to

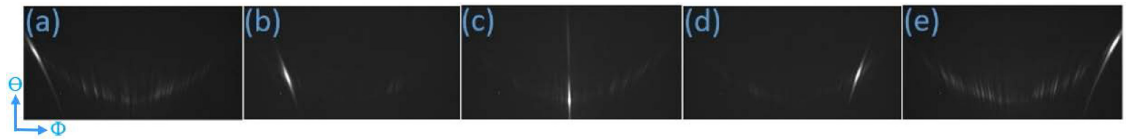

Fig. 10. Some representative spots optimization results of Chip2.

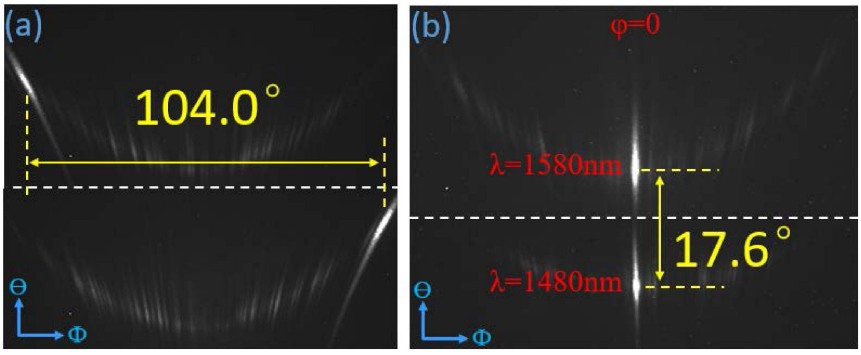

Fig. 11. (a) Lateral scanning range of Chip2. (b) Longitudinal scanning range of Chip2.

the center of the screen, and its light intensity gradually increases. At the same time, the first-order peak moves toward the right side of the screen, and its light intensity gradually decreases. Finally, it disappears from the screen. When φ increases from 0 to a specific value, the first-order peak appears again on the left side of the screen (Fig. 8(g)). It moves toward the right side of the screen along with the zero-order peak, and its intensity gradually increases. When $\varphi = \pi$ (Fig. 8(h)), the first-order peak reaches the same position as the zero-order peak shown in Fig. 8(c). From Fig. 8(c) to (h), φ has changed by 2π. Finally, the intensity of the first-order peak is much stronger than that of the zero-order peak, as shown in Fig. 8(i).

As shown in Fig. 9(a), when the intensity of the main lobe and the grating lobe are equal, we measured the angular distance between them as 46.6°, which is the scanning range of Chip1 in the lateral direction. In addition, the steering angle of its main lobe is 17.5° in the wavelength range of 1480 nm to 1580 nm, as shown in Fig. 9(b).

Then we tested Chip2. Several representative optimization results of the light spots emitted by Chip2 at 1550 nm are shown in Fig. 10. Compared with Chip1, in the test range of the screen, there were no obvious grating lobes in the test of Chip2.

As shown in Fig. 11.(a), we measured the lateral scanning range of Chip2 to be 104.0°, which was much larger than the 46.6° of Chip1. Therefore, reducing the input waveguide spacing of the antenna can greatly increase the scanning range in the lateral direction. In addition, we measured the scanning range of Chip2 in the longitudinal direction as 17.6°, as shown in Fig. 11(b). These test results are basically consistent with the simulation.

We also measured the divergence angles of these spots in the lateral and longitudinal directions. The divergence angles $\Delta\Phi$ of Chip1 and Chip2 in the lateral direction are 0.44° and 0.72°, respectively. However, their divergence angles $\Delta\Theta$ in the longitudinal direction are relatively large, both are about 1.74°. This is because the antenna grating adopted in this article is directly etched on the silicon slab. If the SiN perturbation grating is used [29], the divergence angle of the spot in this direction will be significantly reduced.

Finally, we characterized the loss of the OPA chip. Its total loss is about 10.4 dB, mainly including the input coupler, MMI tree, waveguide and antenna losses of 2.9 dB, 1.5 dB, 1.5 dB and 4.5 dB, respectively. In addition, we experimentally characterized the performance of the phase shifter by

testing the MZ modulator. Its switching power consumption for 2π phase shift is about 12 mW, and its modulation bandwidth is 15 kHz. The steering speed of OPA is mainly determined by the modulation speed of the phase shifter. If the electro-optical phase modulator is used, the power consumption can be smaller and the speed can be faster.

5. Conclusion

We have designed and manufactured two 128-channel silicon-based OPA chips with different input waveguide spacing at the antenna for comparison, and verified that reducing the input waveguide spacing can greatly increase the scanning range of the overall grating antenna in the lateral direction. We have also developed a demo prototype. The spots of its main lobe are clear and consistent with the theory. In addition, a large two-dimensional scanning range of $104.0^\circ \times 17.6^\circ$ is obtained, which is of great significance to promote the practical application of OPA. In the follow-up work, we will carry out long-distance detection research, such as tens and hundreds of meters, to further promote the practical application of OPA.

References

[1] K. V. Acoleyen *et al.*, "Off-chip beam steering with a one-dimensional optical phased array on silicon-on-insulator," *Opt. Lett.*, vol. 34, no. 9, pp. 1477–1479, 2009.

[2] J. K. Doylend, M. J. R. Heck, J. T. Bovington, J. D. Peters, L. A. Coldren, and J. E. Bowers, "Two-dimensional free-space beam steering with an optical phased array on silicon-on-insulator," *Opt. Exp.*, vol. 19, no. 22, pp. 21595–21604, 2011.

[3] A. Yaacobi, J. Sun, M. Moresco, G. Leake, and M. R. Watts, "Integrated phased array for wide-angle beam steering," *Opt. Lett.*, vol. 39, no. 15, pp. 4575–4578, 2014.

[4] D. Kwong, A. Hosseini, J. Covey, Z. Yang, and R. T. Chen, "On-chip silicon optical phased array for two-dimensional beam steering," *Opt. Lett.*, vol. 39, no. 4, pp. 941–944, 2014.

[5] J. C. Hulme, J. K. Doylend, M. J. R. Heck, J. D. Peters, and M. L. Davenport, "Fully integrated hybrid silicon two dimensional beam scanner," *Opt. Exp.*, vol. 23, no. 5, pp. 5861–5874, 2015.

[6] D. N. Hutchison *et al.*, "High-resolution aliasing-free optical beam steering," *Optica*, vol. 3, no. 8, pp. 887–890, 2016.

[7] C. V. Poulton, A. Yaccobi, S. Zhan, M. J. Byrd, and M. R. Watts, "Optical phased array with small spot size, high steering range and grouped cascaded phase shifters," in *Proc. Integr. Photon. Res.*, Silicon & Nanophotonics, 2016, Paper IW1B.2.

[8] R. Manan, C. V. Poulton, and M. R. Watts, "Unidirectional waveguide grating antennas with uniform emission for optical phased arrays," *Opt. Lett.*, vol. 42, no. 13, pp. 2563–2566, 2017.

[9] S. Chung, H. Abediasl, and H. Hashemi, "A monolithically integrated large-scale optical phased array in Silicon-on-Insulator CMOS," *IEEE J. Solid-State Circuits*, vol. 53, no. 1, pp. 275–296, 2018.

[10] C. V. Poulton, M. J. Byrd, E. Timurdogan, P. Russo, D. Vermeulen, and M. R. Watts, "Optical phased arrays for integrated beam steering," in *Proc. IEEE 15th Int. Conf. Group IV Photon. (GFP)*, 2018, pp. 1–2.

[11] P. Wang, Z. Li, H. Yu, Y. Li, and J. Pan, "Improving the performance of the optical antenna for integrated LIDAR with optical phased arrays through high contrast grating structure on SOI substrate," *Ecs Trans.*, vol. 86, pp. 123–130, 2018.

[12] C. V. Poulton *et al.*, "Long-range LiDAR and free-space data communication with high-performance optical phased arrays," *IEEE J. Sel. Topics Quantum Electron.*,vol. 25, no. 5, 2019, Art. no. 7700108.

[13] T. Kim *et al.*, "A single-chip optical phased array in a wafer-scale silicon Photonics/CMOS 3D-Integration platform," *IEEE J. Solid-State Circuits*, vol. 54, no. 11, pp. 3061–3074, 2019.

[14] P. Bhargava *et al.*, "Fully integrated coherent LiDAR in 3D-Integrated silicon Photonics/65nm CMOS," in *Proc. Symp. VLSI Circuits*, 2019, pp. C262–C263.

[15] W. Xie *et al.*, "Heterogeneous silicon photonics sensing for autonomous cars," *Opt. Exp.*, vol. 27, no. 3, p. 3642, 2019.

[16] M. Gehl, G. Hoffman, P. Davids, A. Starbuck, and C. Long, "Phase optimization of a silicon photonic two-dimensional electro-optic phased array," in *Proc. CLEO: Appl. Technol.*, 2019, pp. 1–2.

[17] C. V. Poulton, P. Russo, B. Moss, M. Khandaker, and M. R. Watts, "Small-form-factor optical phased array module for technology adoption in custom applications," in *Proc. CLEO: Appl. Technol.*, 2019, Paper JTh5B.6.

[18] F. Ashtiani, and F. Aflatouni, "N×N optical phased array with 2N phase shifters," *Opt. Exp.*, vol. 27, no. 19, pp. 27183–27190, 2019.

[19] S. A. Miller, Y. C. Chang, C. T. Phare, C. S. Min, and M. Lipson, "Large-scale optical phased array using a low-power multi-pass silicon photonic platform," *Optica*, vol. 7, no. 1, pp. 3–6, 2020.

[20] C. V. Poulton, M. J. Byrd, B. Moss, E. Timurdogan, R. Millman, and M. R. Watts, "8192-element optical phased array with 100° steering range and flip-chip CMOS," in *Proc. Conf. Lasers Electro-Opt.*, WA, DC, 2020, Art. no. JTh4A.3.

[21] B. Behroozpour, P. A. M. Sandborn, M. C. Wu, and B. E. Boser, "Lidar system architectures and circuits," *IEEE Commun. Mag.*, vol. 55, no. 10, pp. 135–142, 2017.

[22] K. V. Acoleyen, H. Rogier, and R. Baets, "Two-dimensional optical phased array antenna on silicon-on-insulator," *Opt. Exp.*, vol. 18, no. 13, 2010, Art. no. 13655.

[23] C. V. Poulton, D. Vermeulen, E. Hosseini, E. Timurdogan, and M. R. Watts, "Lens-free chip-to-chip free-space laser communication link with a silicon photonics optical phased array," in *Proc. Front. Opt.*, 2017, Paper FW5A.3.

[24] C. T. Phare, C. S. Min, S. A. Miller, B. Stern, and M. Lipson, "Silicon optical phased array with high-efficiency beam formation over 180 degree field of view," in *Proc. Conf. Lasers Electro-Optics*, 2018, Paper SM3I.2.
[25] C. V. Poulton, P. Russo, E. Timurdogan, M. Whitson, and M. R. Watts, "High-performance integrated optical phased arrays for chip-scale beam steering and LiDAR," in *CLEO: Appl. Technol.*, 2018, Paper ATu3R.2.
[26] M. J. Byrd, C. V. Poulton, M. Khandaker, E. Timurdogan, and M. R. Watts, "Free-space communication links with transmitting and receiving integrated optical phased arrays," in *Proc. Front. Opt.*, 2018, Paper FTu4E.1.
[27] J. He, T. Dong, and Y. Xu, "Review of photonic integrated optical phased arrays for space optical communication," *IEEE Access*, vol. 8, no. 2169-3536, pp. 188284–188298, 2020.
[28] P. Wang, G. Luo, Y. Xu, Y. Li, and J. Pan, "Design and fabrication of sin-Si Dual-layer optical phased array chip," *Photon. Res.*, vol. 8, no. 6, p. 912, 2020.
[29] M. Zadka, Y.-C. Chang, A. Mohanty, C. T. Phare, S. P. Roberts, and M. Lipson, "On-chip platform for a phased array with minimal beam divergence and wide field-of-view," *Opt. Exp.*, vol. 26, no. 3, pp. 2528–2534, 2018.